Eur. Phys. J. B (2018) 91: 228
https://doi.org/10.1140/epjb/e2018-90091-y

THE EUROPEAN PHYSICAL JOURNAL B

Regular Article

# Electron dynamics on gold surfaces driven by short laser pulses

## An examination of the slab model within the periodic boundary conditions*

Yoshiyuki Miyamoto[a]

Research Center for Computational Design of Advanced Functional Materials, National Institute of Advanced Industrial Science and Technology (AIST), Central 2, 1-1-1 Umezono, Tsukuba, Ibaraki 305-8568, Japan

Received 24 February 2018 / Received in final form 29 June 2018
Published online 3 October 2018


**Abstract.** This paper describes the application of time-dependent density functional theory (TDDFT) to explore dynamics in condensed matter driven by strong short laser pulses. As a specific example, the calculation of the optical response on a gold surface is presented. The real-time TDDFT treatment of metallic systems is difficult due to the presence of a surface of the Fermi level ($E_F$). Depending on $E_F$, the occupation numbers of the states at each of the $k$ points in the wedge of the first Brillouin zone should be assigned to obtain self-consistent charge-density and Kohn–Sham wavefunctions, which are set as the initial condition for the real-time propagation based on TDDFT. Furthermore, a computational scheme for exploring the optical field enhancement by the Au surface and numerical problems arising from the periodic boundary conditions are discussed.

## 1 Introduction

Density functional theory (DFT) [1] with single-particle representation derives the Kohn–Sham equation [2], which reduces the computational cost for studying a variety of materials. By using the total-energy formalism [3] based on the DFT, the mechanical and chemical properties of condensed matter under the electronic ground states can be studied. Furthermore, the continued increase in computing power makes DFT-based molecular dynamics (MD) feasible for studying the thermal properties of condensed matter [4].

Non-equilibrium dynamics in condensed matter have become observable experimentally by employing femtosecond laser techniques [5–7]. Computational methods for understanding and predicting ultra-fast phenomena would thus be of great value. Excited-state MD simulations are a useful tool, yet DFT-based simulations require the two-temperature model for electrons and ions [8], in which both the electrons and ions are thermally equilibrated at different temperatures. However, to investigate very short non-equilibrium responses, real-time propagation for both electrons and ions is necessary. Based on time-dependent DFT (TDDFT) [9], we should be able to study both thermal and non-thermal dynamics of materials conducted by illumination with short laser pulses. The laser field can be expressed as either a vector potential [10] or a dielectric field [11,12].

In this paper, the effect of irradiation with a short-pulse laser field is discussed. Focusing a laser beam increases the laser power, and further power increase can be achieved by compressing the laser beam along the time axis. Advances in experimental technology [13–16] have enabled us to investigate condensed matter using high-power and short-pulse laser beams. It is therefore worthwhile to predict phenomena that will become experimentally accessible in the near future by performing ab initio simulations.

This paper first introduces a TDDFT computational scheme for theoretically studying optical field enhancement [17,18]. Gold (Au) nanoparticles are known to enhance optical fields [19], which is used to improve the Raman signal from solid surfaces [20]. TDDFT was applied in reference [17] to simulate the increased water decomposition near Au nanoparticles, which was approximated using the jellium model. Au atoms contain delocalized orbitals derived from the $6s$ and $6p$ orbitals as well as localized orbitals derived from the $5d$ orbitals. Therefore, the suitability of the jellium model in this case is debatable, and atomic-scale calculations seem to be necessary. However, the size of these nanoclusters appears to be too large to allow the use of atomic-scale real-time propagation TDDFT calculations to examine the optical field enhancement. Instead, in this study, a slab model based on an Au(111) surface with a thickness of about 2 nm was

* Contribution to the Topical Issue "Special issue in honor of Hardy Gross", edited by C.A. Ullrich, F.M.S. Nogueira, A. Rubio, and M.A.L. Marques.

[a] e-mail: yoshi-miyamoto@aist.go.jp

employed to examine the optical field enhancement near the surface.

This paper is organized as follows. The computational scheme is described in Section 2, and the necessary considerations for real-time TDDFT calculations of metallic systems are discussed in Section 3. The results are presented in Section 4, and a summary is provided in Section 5.

## 2 Computational schemes

All of the calculations presented here are based on the real-time propagation scheme of the TDDFT using the Suzuki–Trotter split operator [21,22]. A plane-wave code [23,24] using the split-operator scheme was used. Norm-conserving pseudopotentials [25] in the separable form [26] were used to implement the split-operator methods in the plane-wave code.

Under a laser field, we solve the time-dependent Kohn–Sham equation,

$$i\hbar\frac{\partial\psi_n^{\mathrm{KS}}(\mathbf{r},t)}{\partial t} = \left[H^{\mathrm{KS}}[\rho(\mathbf{r},t)] + V_{\mathrm{ext}}(\mathbf{r},t)\right]\psi_n^{\mathrm{KS}}(\mathbf{r},t), \quad (1)$$

where $\psi_n^{\mathrm{KS}}(\mathbf{r},t)$ represents the time-dependent Kohn–Sham orbital with quantum state index $n$. $H^{\mathrm{KS}}[\rho(\mathbf{r},t)]$ is the Kohn–Sham Hamiltonian containing the exchange-correlation potential as a function of the charge density $\rho(\mathbf{r},t)$, which is the sum of the norm of all of the Kohn–Sham orbitals with occupied states $n$. $V_{\mathrm{ext}}(\mathbf{r},t)$ is a time-varying scalar potential that expresses the optical field $\mathbf{E}(\mathbf{r},t)$ as

$$\mathbf{E}(\mathbf{r},t) = -\frac{\partial V_{\mathrm{ext}}(\mathbf{r},t)}{\partial \mathbf{r}}. \quad (2)$$

Since the plane-wave basis set is used, we need to employ a unit cell for the three-dimensional periodic boundary conditions. With introduction of the vacuum region in the unit cell, $V_{\mathrm{ext}}(\mathbf{r},t)$ can also be periodic by changing its polarity at the vacuum region (this is referred to as the "sawtooth scheme"). By introducing a fictitious charge density $\rho_{\mathrm{ext}}(\mathbf{r},t)$ that is neutral after taking the integral over the unit cell, we obtain

$$V_{\mathrm{ext}}(\mathbf{r},t) = \int\frac{\rho_{\mathrm{ext}}(\mathbf{r}',t)}{\mid\mathbf{r}-\mathbf{r}'\mid}d\mathbf{r}'. \quad (3)$$

The introduction of $\rho_{\mathrm{ext}}(\mathbf{r})$ changes the formula of the total energy (potential energy) as follows:

$$\begin{aligned}E_{\mathrm{tot}}^{\mathrm{TDDFT}}(t) = {}& \frac{-\hbar^2}{2m}\int\psi_n^{\mathrm{KS}*}(\mathbf{r},t)\frac{\partial^2}{\partial\mathbf{r}^2}\psi_n^{\mathrm{KS}}(\mathbf{r},t)d\mathbf{r}\\ &+\int\int\psi_n^{\mathrm{KS}*}(\mathbf{r}',t)v_{nl}^{pp}(\mathbf{r}',\mathbf{r},t)\psi_n^{\mathrm{KS}}(\mathbf{r},t)d\mathbf{r}d\mathbf{r}'\\ &+\frac{1}{2}\int\int\frac{(\rho(\mathbf{r}',t)+\rho_{\mathrm{ext}}(\mathbf{r}',t))\,(\rho(\mathbf{r},t)+\rho_{\mathrm{ext}}(\mathbf{r},t))}{\mid\mathbf{r}'-\mathbf{r}\mid}d\mathbf{r}'d\mathbf{r}\\ &+\sum_I Z_I\int\frac{\rho(\mathbf{r},t)+\rho_{\mathrm{ext}}(\mathbf{r},t)}{\mid\mathbf{r}-\mathbf{R}_I(t)\mid}d\mathbf{r}\\ &+\int E_{\mathrm{HXC}}[\rho(\mathbf{r},t)]\rho(\mathbf{r},t)d\mathbf{r}+\sum_{I\neq J}\frac{Z_IZ_J}{\mid\mathbf{R}_I(t)-\mathbf{R}_J(t)\mid}. \quad (4)\end{aligned}$$

The first and second terms of equation (4) represent the contributions from the electron kinetic energy and the sum of all non-local pseudopotentials $v_{\mathrm{nl}}^{\mathrm{pp}}(\mathbf{r}',\mathbf{r},t)$, respectively. The final two terms represent the contributions of the exchange-correlation potential and ion–ion Coulomb repulsion. Here, index $I$ and $Z_I$ represent each ion and its valence charge. The third and fourth terms express the electron–electron Coulomb term (Hartree term) and the electron–ion Coulomb term, respectively, which are modulated to include the interaction of the light with the electrons and ions. Since the integral of $\rho_{\mathrm{ext}}(\mathbf{r},t)$ over the unit cell is set to zero, the total energy per unit cell does not diverge and the momentum-space formalisms of the total energy [3] can be applied as well as the formalism to compute force on each ion $I$ ($\mathbf{F}_I(t)$). Then Newton's equation of motions

$$M_I\frac{d^2\mathbf{R}_I(t)}{dt^2} = \mathbf{F}_I(t), \quad (5)$$

was applied for all ion motion. Here $M_I$, $\mathbf{R}_I(t)$ respectively denote mass and position of ion $I$. The equations (1) for electrons and (5) for ions were solved simultaneously with common interval of the time-step in performing the Ehrenfest dynamics. From solutions of equation (5), one can obtain kinetic energies of ions as

$$E_I^{\mathrm{kin}}(t) = \frac{1}{2}M_I\left(\frac{d\mathbf{R}_I(t)}{dt}\right)^2. \quad (6)$$

When the exchange-correlation energy $E_{\mathrm{HXC}}[\rho(\mathbf{r},t)]$ is assumed as a local functional with respect to time $t$, the sum of the total energy and kinetic energy of all of the ions per unit cell, $U(t) \equiv E_{\mathrm{tot}}^{\mathrm{TDDFT}}(t) + \sum_I E_I^{\mathrm{kin}}(t)$, is conserved in the absence of an optical field (i.e., without $\rho_{\mathrm{ext}}(\mathbf{r},t)$). However, when the optical field is non-zero, $U(t) - W(t)$ is conserved, in which $W(t)$ represents the work done by the optical field, and its time derivative is given as follows [27]:

$$\begin{aligned}\frac{\partial W(t)}{\partial t} = \int\frac{\partial\rho_{\mathrm{ext}}(\mathbf{r},t)}{\partial t}\left(\int\frac{\rho(\mathbf{r}',t)+\rho_{\mathrm{ext}}(\mathbf{r}',t)}{\mid\mathbf{r}'-\mathbf{r}\mid}d\mathbf{r}'\right.\\ \left.+\sum_I\frac{Z_I}{\mid\mathbf{r}-\mathbf{R}_I\mid}\right)d\mathbf{r}. \quad (7)\end{aligned}$$

Note that equation (7) can be numerically computed within the scheme of the momentum-space formalism [3]. At the moment when $\rho_{\mathrm{ext}}(\mathbf{r},t)$ becomes zero, $E_{\mathrm{tot}}^{\mathrm{TDDFT}}(t)$ expresses the potential energy of the system increased by optical excitation.

## 3 Computational scheme for TDDFT calculations of metallic systems

In this section, a practical scheme for performing TDDFT on Au surfaces is presented. In Section 3.1, the considerations for assigning occupation numbers for each

state are addressed. In Section 3.2, the utility of the norm-conserving pseudopotentials [25] is discussed.

### 3.1 Assigning occupation numbers for metallic systems

Real-time propagation TDDFT is performed keeping the self-consistent field (SCF) between the Kohn–Sham orbitals and Hamiltonian by using fixed occupation numbers that are determined when preparing the initial condition of the simulation. When the initial state is an optically excited state employing the constraint DFT (ΔSCF) scheme [28], electrons must be promoted from an occupied level to an unoccupied level to proceed with the SCF calculation to solve the Kohn–Sham equation. In contrast, as in the current case, when the initial condition is an electronic ground state, an ordinary DFT calculation can be performed in which the geometry is optimized to minimize the total energy. Throughout the real-time evolution of the TDDFT, in the presence of a dynamic external field or lattice dynamics, the occupation numbers are fixed. However, fixing the occupation number does not restrict the simulation to remain at a particular adiabatic potential energy surface (PES) since the Kohn–Sham orbitals are free to change their characteristics from those of the occupied states to those of the unoccupied states throughout the time propagation.

The above-mentioned scheme is applicable to systems with an energy gap as well as metallic systems. In periodic systems, the Kohn–Sham orbitals have the characteristics of Bloch functions with $k$ vectors. In metallic system, by taking finite numbers of $k$ vectors as sampling points for the integration over the momentum space, one must assign an occupation number for each $k$ point by referring to the position of the Fermi level ($E_F$), as determined using a scheme for simulating metallic systems such as that reported in reference [29]. The smearing technique assuming finite electron temperature was not applied to avoid any effect of electronic excitation besides laser field. The eigenstates below $E_F$ should be assigned as occupied, while those above $E_F$ should be empty. There should also be degenerate eigenlevels near $E_F$, for which fractional occupation numbers should be assigned.

### 3.2 Checking Troullier–Martins pseudopotentials and numerical conditions for gold

The Troullier–Martins (TM) type norm-conserving pseudopotentials [25] in the separable form [26] are indispensable for minimizing the computational cost of real-time TDDFT calculations. The utility of the norm-conserving pseudopotentials for solid Au was demonstrated by tuning the parameter sets for the recommend form for the local reference potential [30,31] as well as the core radii, beyond which the "true" and "pseudo" wavefunctions for an isolated Au atom match. The plane-wave basis set with a kinetic cutoff energy of 120 Ry was used. In current scheme, the semicore-state was not included.

The lattice constant, bulk modulus, and band dispersion of fcc Au were computed, as shown in Figure 1. As depicted in Figure 1a, the calculated lattice constant was 2% higher than the experimental value and the calculated bulk modulus was 18% higher than those reported experimentally [32], as determined using the local-density approximation (LDA) with a functional [33] fitted to the numerical data for a uniform gas [34]. Calculations based on the generalized gradient approximation (GGA) within the Perdew–Burke–Ernzerhof (PBE) functional [35] were also tested but afforded inferior accuracy for the lattice constant and the bulk modulus than LDA, so the latter was chosen for this study. In addition, Figure 1b shows the computed band structure; The band dispersion near $E_F$ agrees reasonably well with the previous calculations based on many-body perturbation theory [36], while there are discrepancy in inter-band excitation energy.

## 4 Optical response of the Au(111) surface

To address the optical field enhancement, a repeating slab model with a (111) surface was examined. Here, a nine-layer slab model as depicted in Figure 2 was employed. The $1 \times 1$ periodic boundary was taken in the directions parallel to the surface. The theoretical lattice constant was used to construct this model. For the momentum-space integration, 12 $k$ points were used for an irreducible wedge of the surface Brillouin zone under $C_{3v}$ symmetric conditions. (Because of the presence of an oscillating $E$ field, inversion with respect to the surface-normal direction was omitted.) This $k$-point sampling corresponds to the use of 108 $k$ points in the first Brillouin zone. All of the atoms were fully relaxed toward the total-energy minimum under the electronic ground states. For the geometry optimization, a vacuum region with 14.72 Å thickness was introduced. For comparison, some calculations were also performed with a vacuum region of 20.72 Å. These numerical conditions were used to calculate the optical absorption spectrum and examine the optical field enhancement.

### 4.1 Optical spectroscopy with surface-normal polarization

The photo-absorption spectrum of an Au(111) surface was computed with the polarization vector normal to the surface by applying the scheme reported in reference [37]. It is well known that the surface-parallel component of an optical field is screened by the metallic surface whereas the surface-normal component is not. Therefore, in this work, the optical response to light with surface-normal polarization was examined. In practice, the surface-normal component of the optical field is realized with an off-normal light incident angle with the p-polarization condition, in which the optical field is in the plane consisting of the incident vector of the light and the surface-normal vector.

The following procedure was performed. After applying a single short Gaussian pulse of 0.5 fs, the time evolution of the generated dipole

$$\mathbf{P}(t) = \int \rho(\mathbf{r}, t)(\mathbf{r} - \mathbf{r}_0)d\mathbf{r}, \tag{8}$$

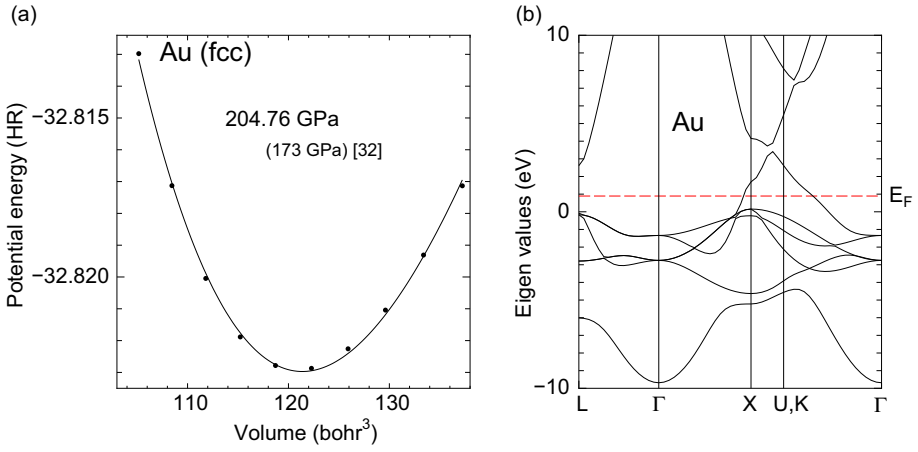


**Fig. 1.** (a) Potential–volume plot for the fcc phase of Au. The computed bulk modulus was obtained from a second-order Birch–Murnaghan fitting curve (solid line). The value of bulk modulus 173 GPa is recent experimental report [32]. (b) Energy band structure for the fcc phase of Au with a theoretical lattice constant. The location of $E_F$ is denoted by the horizontal dashed red line. These calculations were performed using the LDA with the Troullier–Martins-type norm-conserving pseudopotentials; see the main text for details.

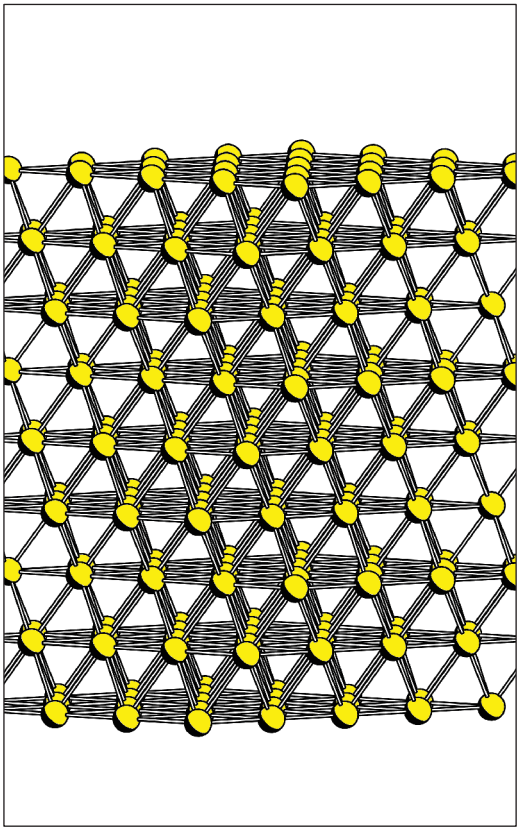

**Fig. 2.** Slab model for the Au(111) surface viewed from near a surface parallel direction. The thickness of the slab corresponds to nine atomic layers (18.94 Å) and all of the atoms were relaxed toward the total-energy minimization.

was monitored. The finite-time Fourier transformation was taken for $\mathbf{P}(t) - \mathbf{P}(t = 0)$ to extract the frequency domain required for computing the absorption intensity as a function of the photon energy.

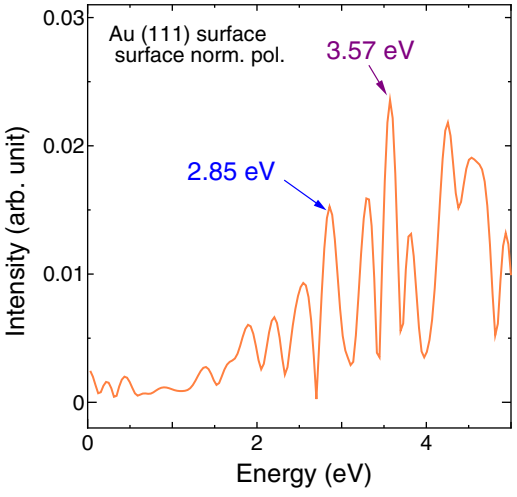


**Fig. 3.** Calculated photo-absorption spectrum of the Au(111) surface with surface-normal optical polarization. The arrow labeled 2.85 eV indicates the strongest absorption peak in the visible region, while the arrow labeled 3.57 eV indicates a peak in the UV region.

Figure 3 shows the optical absorption peaks obtained from the TDDFT calculations. The finite-time Fourier transformation was obtained up to $t = 37$ fs (the initial signal up to 2 fs was omitted to avoid noise). A fairly large peak was observed in the visible region at 2.85 eV, which corresponds to a blue color. As for the light reflection, the reflected light lacked the blue component, which causes the color of the Au(111) surface to appear yellow.

### 4.2 Optical field calculation near the Ag(111) surface and associated numerical problems

The electric field (E field) induced by light was calculated at positions 3 Å above the top surface of the slab and 3 Å below the bottom surface of the slab. Since there are

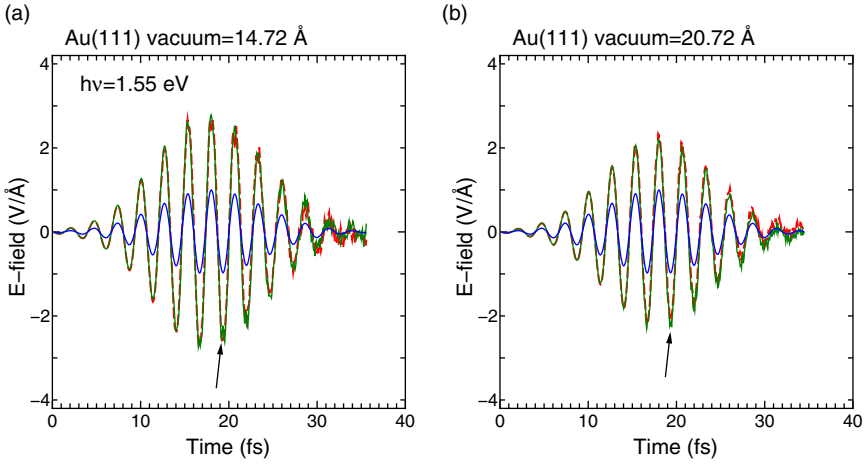


**Fig. 4.** Optical responses of the Au(111) surface with a photon energy of 1.55 eV and a pulse width (FWHM) of 10 fs for the E-field intensity. The time evolution of the applied field is represented by the solid blue line, and the generated E fields 3 Å above the top surface and 3 Å below the bottom surface of the slab are represented by the dashed red line and solid green line, respectively. The calculations were performed with vacuum regions of (a) 14.72 Å and (b) 20.72 Å. The arrows indicate the time point of 19.24 fs, at which the snapshots shown in Figure 5 were taken.

persistently finite values of the E field at these positions, the time differences $\mathbf{E}(t) - \mathbf{E}(t = 0)$ are plotted. The three typical photon energies of 1.55, 2.85, and 3.57 eV, two of which occurred as peaks in Figure 3, were selected as case studies, and the full width at half-maximum (FWHM) of the optical E field was set as 10 fs. The maximum intensity of the E field was set as 1 V/Å. By performing the TDDFT Ehrenfest MD simulation with zero initial velocities of all ions, the Au(111) surface was found to be unchanged up to 40 fs.

It should be noted that the optical field near the Au(111) surface should be enhanced when the optical frequency matches the resonance excitation observed in Figure 3; however, as shown in Figure 4a, enhancement also occurred when the photon energy was off-resonance (1.55 eV) with the corresponding wavelength of 800 nm. Figure 4a shows that the induced E field 3 Å above (below) the top (bottom) surface of the slab increased by a factor of three compared with the intensity of the applied optical field. Such a large increase seems to explain the light enhancement effect previously observed for gold nanoparticles [17,19]; however, the calculated enhancement factor decreases as the vacuum region increases, as shown in Figure 4b.

The cause of the dependence on the vacuum region in the periodic boundary condition was understood from snapshots of the SCF potential profile along the surface-normal direction. The atomic-scale variation of the SCF potential was smeared out by taking the difference of the time-varying SCF potential obtained by TDDFT and that obtained by static DFT as

$$V_{\mathrm{SCF}}^{\mathrm{TDDFT}}(z,t) - V_{\mathrm{SCF}}^{\mathrm{DFT}}(z), \tag{9}$$

where $z$ represents the surface-normal axis. The potential was averaged in the surface-parallel direction.

Figure 5 shows the potential profiles with the vacuum regions of 14.72 and 20.72 Å. Panels (a) and (b) of

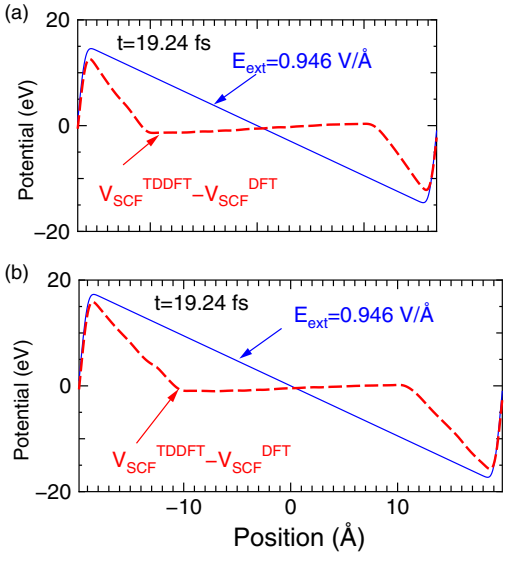


**Fig. 5.** Snapshots at $t = 19.24$ fs of the potential profiles obtained by the optical field (solid blue lines) with photon energy of 1.55 eV and the SCF potential (dashed red lines) along the surface-normal direction. The origin of each panel is the center position of the slab. The atomic-scale variation of the SCF potential was smeared out by the method described in the main text. The top (a) and bottom (b) panels show the cases with vacuum regions of 14.72 and 20.72 Å, respectively, with common scales in lateral and vertical axes. A frame of panel (a) is smaller than (b) due to smaller vacuum region, and the left and right ends of these panels are the periodic boundaries in the surface-normal direction.

Figure 5 are drawn in common scale thus in different size due to different vacuum regions. The slope of the potential profile becomes less pronounced inside the Au slab due to the screening nature of the metal. Because of this screening, the bias across the slab becomes small, and thus the

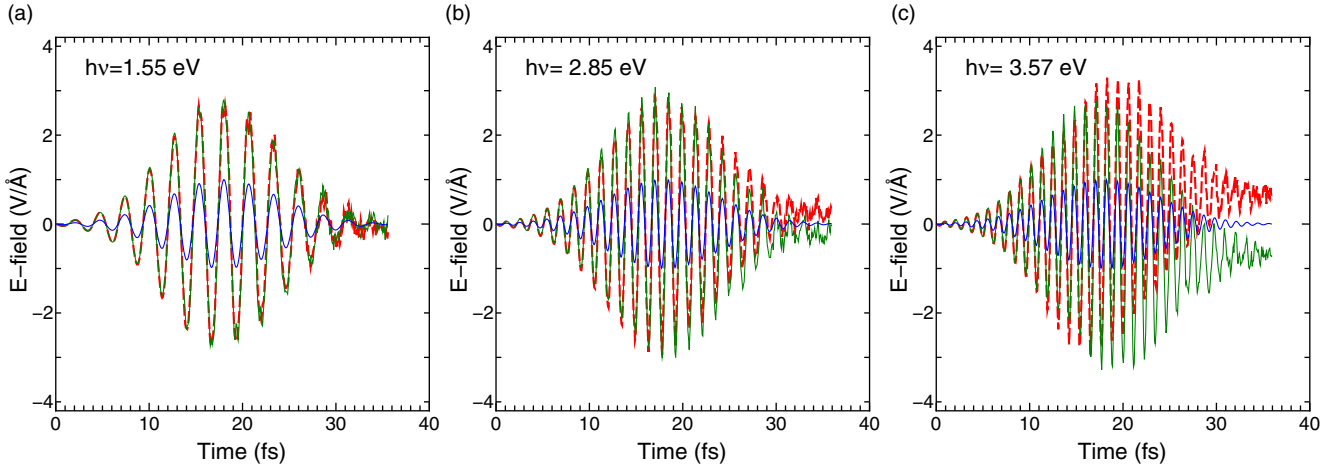


**Fig. 6.** Photon-energy dependence of the optical response of the Au(111) surface using a vacuum region of 14.72 Å. The plots show the applied and induced E fields at photon energies of (a) 1.55 eV (the same as Fig. 4a), (b) 2.85 eV, and (c) 3.57 eV. The solid blue lines represent the applied E field, and the dashed red lines and solid green lines represent the induced E fields 3 Å above the top surface and 3 Å below below the bottom surface of the slab, respectively.

bias in the vacuum region becomes large to maintain consistency with the applied bias near the end of the periodic boundary condition. This is an artificial effect that arises from the periodic boundary conditions and can be avoided when the vacuum region is thicker than the slab in terms of magnitude. Current slab model has a thickness of 18.94 Å, and thus the vacuum region of 20.72 Å is still insufficient to avoid the appearance of an artificially strong field near the surface. At present, it is difficult to perform real-time propagation using a thick vacuum region with increasing slab thickness owing to the computational cost.

Finally, the dependence of the optical response of the Au(111) surface on the photon energy was examined using a vacuum region of 14.72 Å. The photon energies of 2.85 and 3.57 eV, which occurred as absorption peaks in Figure 3, were tested. Figure 6 shows the numerical results, where the solid blue lines represent the applied E field and the dashed red lines and solid green lines represent the induced E fields 3 Å above the top surface and 3 Å below the bottom surface of the slab model, respectively. At the photon energy of 2.85 eV, the amplitude of the induced E field did not exhibit a significant difference from that of the off-resonance case, as shown in Figure 6a. In contrast, at the photon energy of 3.57 eV, the induced E field showed a persistent change in the center of mass of the oscillating E field. This persistent change suggests the charging up of the slab, that is, photoemission of electrons from the Au(111) surface. However, we must remind that the work function of Au exceeds 5 eV [38]. The current potential profile show enough increase of energy from slab to vacuum being consistent to the value of the work function. Therefore, the photo-emission of valence electrons is very likely to be milti-photon process due to strong optical field. Otherwise, the electron tunneling may occur within current vacuum region. (Note that the technique to treat electron absorption at the boundary was not applied in current simulation.) Besides the persistent change, at the photon energy of 3.57 eV, the amplitude of the oscillation of the induced E field did not show a significant change from that of the off-resonance condition shown in Figure 6a. It is therefore concluded that the current calculations based on the slab model do not precisely account for the optical field enhancement reported for Au nanoclusters [19].

## 5 Summary

A real-time TDDFT scheme for metallic systems has been presented. The assignment of the occupation numbers should be made dependent on the sampled $k$ points in the wedge of the first Brillouin zone according to the computed value of $E_F$. The utility of the TM pseudopotentials was evaluated for the case of Au by examining the lattice constant, bulk modulus, and band dispersion. In the current study, LDA afforded superior results than PBE. Based on the computations of the optically enhanced E field, an artifact arising from the periodic boundary conditions was discussed and the vacuum region must far exceed the slab thickness for numerically reliable estimations. The current slab simulations do not fully account for the significant E-field enhancement regardless of whether the photon energy is resonant with the absorption peak, and further simulations of Au clusters using a larger computational size would be desirable.

This work was financially supported by JSPS KAKENHI under grant numbers JP16K05049, JP16H00925, JP16K05412, and JP16H04103. All of the computations were performed using the supercomputer system at the Cyberscience Center of Tohoku University.

## Author contribution statement

The author was involved in the preparation of the manuscript and corresponding numerical data.

## References


1. P. Hohenberg, W. Kohn, Phys. Rev. **136**, B864 (1964)
2. W. Kohn, L. Sham, Phys. Rev. **140**, A1133 (1965)
3. J. Ihm, A. Zunger, M.L. Cohen, Phys. C **12**, 4409 (1979)
4. O. Sugino, R. Car, Phys. Rev. Lett. **74**, 1823 (1995)
5. N. Bloembergen, A.H. Zewail, J. Phys. Chem. **88**, 5459 (1984)
6. R.N. Zare, Science **279**, 1875 (1998)
7. Y.J. Shiu, Y. Shi, M. Hayashi, C. Su, K.L. Han, S.H. Lin, Chem. Phys. Lett. **378**, 202 (2003)
8. Z. Lin, L.V. Zhigilei, Proc. of SPIE, High-Power Laser Ablation VI **6261**, 62610U (2006)
9. E. Runge, E.K.U. Gross, Phys. Rev. Lett. **52**, 997 (1984)
10. K. Yabana, S. T, Y. Shinohara, T. Otobe, G.F. Bertsch, Phys. Rev. B **85**, 045134 (2012)
11. A. Castro, M.A.L. Marques, J.A. Alonso, G.F. Bertsch, A. Rubio, Eur Phys. J. D **28**, 211 (2004)
12. A. Castro, A. Heiko, O. Micael, A.R. Carlo, X. Andrade, F. Lorenzen, M.A.L. Marques, E.K.U. Gross, A. Rubio, Phys. Status Solidi B **243**, 2465 (2006)
13. H. Niikura, F. Légare, R. Hasbani, A.D. Bandrauk, M.Y. Ivanov, D.M. Villeneuve, P.B. Corkum, Nature **417**, 917 (2002)
14. Y. Shimotsuma, K. Hirao, P.G. Kazansky, J. Qiu, Jpn. J. Appl. Phys. **44**, 4735 (2005)
15. A. Hu, Y. Zhou, W.W. Duley, Open Surf. Sci. J. **3**, 42 (2011)
16. S. Richter, S. Döring, A. Tünnermann, S. Nolte, Appl. Phys. A **103**, 257 (2011)
17. L. Yan, F. Wang, S. Meng, ACS Nano **10**, 5452 (2016)
18. Y. Miyamoto, H. Zhang, X. Cheng, A. Rubio, Phys. Rev. B **96**, 115451 (2017)
19. S. Eustis, M.A. El-Sayed, Chem. Soc. Rev. **35**, 209 (2006)
20. J.F. Li et al., Nature **464**, 392 (2010)
21. M. Suzuki, J. Phys. Soc. Jpn. **61**, 3015 (1992)
22. M. Suzuki, T. Yamauchi, J. Math. Phys. **34**, 4892 (1993)
23. O. Sugino, Y. Miyamoto, Phys. Rev. B **59**, 2579 (1999)
24. O. Sugino, Y. Miyamoto, Phys. Rev. B **88**, 089901(E) (2002)
25. N. Troullier, J.L. Martins, Phys. Rev. B **43**, 1993 (1991)
26. L. Kleinman, D.M. Bylander, Phys. Rev. B **48**, 1425 (1982)
27. Y. Miyamoto, H. Zhang, Phys. Rev. B **77**, 165123 (2008)
28. R.G. Parr, W. Yang, *Density-Functional Theory of Atoms and Molecules* (Oxford University Press, New York, 1989)
29. P.E. Blöchl, O. Jepsen, O.K. Andersen, Phys. Rev. B **49**, 16223 (1994)
30. K. Kobayashi, Comput. Mater. Sci. **14**, 72 (1999)
31. K. Kobayashi, Mater. Trans. **42**, 2153 (2001)
32. A. Yoneda, H. Fukui, H. Gomi, S. Kamada, L. Xie, N. Hirao, H. Uchiyama, S. Tsutsui, A.Q.R. Baron, Jpn. J. Appl. Phys. **56**, 095801 (2017)
33. J.P. Perdew, A. Zunger, Phys. Rev. B **23**, 5048 (1981)
34. D.M. Ceperley, B.J. Alder, Phys. Rev. Lett. **45**, 566 (1980)
35. J.P. Perdew, K. Burke, M. Ernzerhof, Phys. Rev. Lett. **77**, 3865 (1996)
36. T. Rangel, D. Keeik, P.E. Trevisanutto, G.M. Rignanese, H.V. Swygenhoven, V. Olevano, Phys. Rev. B **86**, 125125 (2012)
37. K. Yabana, G.F. Bertsch, Phys. Rev. B **54**, 4484 (1996)
38. W.M.H. Sachtler, G.J.H. Dorgelo, A.A. Holscher, Surf. Sci. **3**, 221 (1966)